

Estimating the Localizability in Tunnel-like Environments using LiDAR and UWB

Weikun Zhen Sebastian Scherer

Abstract—The application of robots in inspection tasks has been growing quickly thanks to the advancements in autonomous navigation technology, especially the robot localization techniques in GPS-denied environments. Although many methods have been proposed to localize a robot using onboard sensors such as cameras and LiDARs, achieving robust localization in *geometrically degenerated* environments, e.g. tunnels, remains a challenging problem. In this work, we focus on the robust localization problem in such situations. A novel degeneration characterization model is presented to estimate the *localizability* at a given location in the prior map. And the localizability of a LiDAR and an Ultra-Wideband (UWB) ranging radio is analyzed. Additionally, a probabilistic sensor fusion method is developed to combine IMU, LiDAR and the UWB. Experiment results show that this method allows for robust localization inside a long straight tunnel.

I. INTRODUCTION

In this work, we aim to address the robust localization problem in robot-based tunnel inspection tasks. Compared with traditional human-based approaches, robots are more flexible and efficient in that they do not require specialized tools to gain mobility, and are able to access places that are dangerous for humans. Recent advancements in robot sensing and autonomous navigation have significantly increased the usage of robots in such applications. However, as one of the most fundamental problems, localizing a robot inside long straight tunnels remains challenging even for the state-of-the-art methods. Reasons for localization failure include darkness, dust, ambiguity and so on. Here we focus on the ambiguity issue faced by most LiDAR-based systems.

To localize a robot in situations where system reliability is critical, LiDARs are more widely used than other sensors thanks to its long-ranging capacity and robustness to low illumination conditions. However, since a LiDAR captures the geometry information by scanning the environment, it is more likely to be affected in geometrically degenerated cases. For example, a robot navigating through a long straight tunnel (as seen in Fig. 1 top-left) will not be able to determine its location along the tunnel since the measurements are identical everywhere. We can understand the degeneration with an analogy to a sliding block inside a pipe (see Fig. 1 bottom-left). The block is obtained by connecting the endpoints of the LiDAR scan. The contact forces, analogous to the surface normals, prohibit motions towards the sides of the pipe. However, since there is no friction to restrain the object, its motion along the pipe becomes under-constrained.

Weikun Zhen is with the Department of Mechanical Engineering, Carnegie Mellon University, weikunz@andrew.cmu.edu

Sebastian Scherer is with the Robotics Institute of Carnegie Mellon University, basti@andrew.cmu.edu

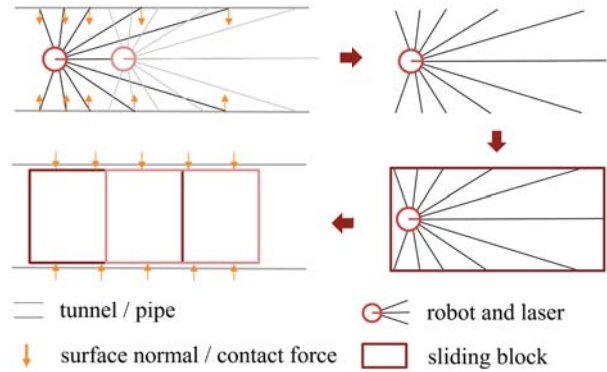


Fig. 1: An analogy between robot navigation inside a tunnel and a sliding block inside a pipe, where the measured surface normals correspond to contact forces.

To identify the geometric degeneration in general environments, a mathematical model to predict the localizability is needed. Besides, a mathematical model can also assist in actively placing sensors to eliminate the degeneration. In this work, we first formulate the localizability model from a set of geometric constraints, then compare the localizability of the LiDAR and the UWB, showing that the two sensors are complementary in constraining the pose estimation problem. Finally, the UWB ranging information is fused with a rotating 2D LiDAR in a probabilistic filtering framework. In experiments, we show that the incorporation of a single UWB ranging radio can significantly improve the localization performance inside a tunnel.

The main contribution of this paper is a novel localizability estimation method that is easy to implement and has a physically meaningful metric. We believe this model is useful for sensing system design, active perception/sensing and path planning to minimize the risk of localization failure. As the secondary contribution, we present a simple probabilistic sensor fusion method that combines a UWB ranging radio with the IMU-LiDAR system for accurate localization.

The rest of this paper is organized as follows: Section II discusses related work on localizability estimation, while Section III describes the proposed localizability model and the sensor fusion method in detail. The experimental results are presented in Section IV. Finally, the paper is concluded in Section V.

II. RELATED WORK

There is plenty of work modeling the sensor localizability, observability or uncertainty. Those approaches can be cate-

gorized by the type of sensors. For LiDAR-based approaches, perhaps the earliest attempt is from Roy and Thrun [1], which is known as *coastal navigation*. Their model is formulated in a probabilistic framework but needs approximations to compute the uncertainty efficiently. Instead of modeling the laser uncertainty directly, Diosi and Kleeman [2] compute the uncertainty of line segments extracted from laser scans. Censi [3] derives a lower bound of the uncertainty matrix that 2D ICP algorithms can achieve using Cremar-Rao's bound, which actually inspires the development of our method. His later work extends the idea to pose tracking [4] and localization [5]. Liu et al. [6] provide a numerical implementation of this approach in 2D and a planner is developed to maximize the determinant of the computed information matrix. Similarly, methods that apply the concept of localizability to design optimal planners are proposed in [7], [8] and [9]. Zhang et al. [10] use a *degeneracy factor* to characterize geometric degeneration and improve the accuracy of ego-motion estimation in the context of solving an optimization problem. Our previous work [11] describes a simple method that builds an information matrix from 3D normal vectors and use its eigenvalues to measure the localizability. However, it only considers translation and does not provide an explanation for the metric of localizability. Different from the methods mentioned before which are mostly derived using geometric rules, Vega et al. [12] propose a learning approach to predict uncertainty matrix based on the system's experience. This approach is demonstrated using cameras and LiDARs in the simulation. In the case of cameras, available approaches typically try to estimate the uncertainty of extracted features. For example, Eudes and Lhuillier [13] model the error propagation from image pixels to reconstructed 3D points in the settings of a bundle adjustment problem. Our Localizability model shares a similar idea with [4] and [10] in that the sensitivity of measurements w.r.t. parameters is used to identify degeneration. But we formulate the sensitivity from a constraint set and use a different but physically meaningful metric to evaluate the localizability.

People have also proposed approaches for reliable localization in tunnels. For example, monocular camera [14], or camera-LiDAR [15] systems are used to provide state estimation for the robot inside a pipe or tunnel. However, those methods may not work in the absence of visual or structural features. Differently, [16] and [17] present a localization method using the periodic radio frequency signal fading, which achieves an accuracy of half the fading period. Besides, Kim et al. [18] use UWB for localization inside tunnels. Those approaches are more robust to low-texture and geometrically degenerated conditions and are similar to our localization approach. But our work is focused on localizability estimation which allows for appropriate selection or placement of sensors.

III. APPROACH

In this section, we first present the formulation of the proposed geometric degeneration model and then elaborate on the IMU, LiDAR and UWB fusion algorithm. Throughout

the paper, bold lower-case letters (e.g. \mathbf{x}) represent vectors and bold upper-case letters (e.g. \mathbf{R}) represent matrices. Scalars are denoted as light lower-case letters (e.g. ρ). In formulations related to probabilistic sensor fusion, we use the symbols $\bar{\cdot}$ and $\tilde{\cdot}$ to indicate the prior and the observation respectively, while the posterior does not have a header.

A. The Degeneration of Geometry

The goal of modeling the degeneration of geometry is to develop theoretical tools to identify degeneration in given maps and also gain insights on designing reliable sensing systems. In other words, given the prior map, we would like to answer whether the current measurement from a specific sensor contains enough information to estimate the robot state.

1) *Localizability of the LiDAR*: First of all, we represent the LiDAR-based localization problem as solving a set of constraint equations:

$$\mathcal{C}(\mathbf{x}, \mathbf{R}, \rho_i) = \mathbf{n}_i^T (\mathbf{x} + \mathbf{R} \mathbf{r}_i \rho_i) + d_i = 0 \quad (1)$$

where $(\mathbf{x}, \mathbf{R}) \in (\mathbb{R}^3, SO(3))$ denotes the robot position and orientation, and $i \in \{1, 2, \dots, m\}$ is the point index in the laser scan. $(\mathbf{n}_i, d_i) \in (\mathbb{R}^3, \mathbb{R})$ encodes the normal vector and distance which is estimated by fitting a local plane to the neighboring points. $\mathbf{r}_i \in \mathbb{R}^3$ is the unit range vector represented in the robot body frame and $\rho_i \in \mathbb{R}$ is the range value. Eqn. 1 describes a simple fact that the scanned points should align with the map when the robot is localized.

Now we evaluate the *strength* of the constraint by measuring the sensitivity of measurements w.r.t. the robot pose. The key observation is that if the robot pose is perturbed slightly but the resulting measurements do not change much, then the constraint is weak. Otherwise, the constraint is strong. Therefore, it is natural to compute the derivative of ρ_i w.r.t. \mathbf{x} and \mathbf{R} as a measure of the sensitivity. Stacking the derivatives computed from all the constraints gives two matrices:

$$\mathbf{F} = \begin{bmatrix} -\frac{\mathbf{n}_1}{\mathbf{n}_1^T \mathbf{r}_1} & \dots & -\frac{\mathbf{n}_m}{\mathbf{n}_m^T \mathbf{r}_m} \end{bmatrix} \quad (2)$$

$$\mathbf{T} = \begin{bmatrix} -\frac{\rho_1 \mathbf{r}_1 \times \mathbf{n}_1}{\mathbf{n}_1^T \mathbf{r}_1} & \dots & -\frac{\rho_m \mathbf{r}_m \times \mathbf{n}_m}{\mathbf{n}_m^T \mathbf{r}_m} \end{bmatrix} \quad (3)$$

(see Appendix I for details). We could then perform Eigenvalue Decomposition on the information matrices:

$$\mathbf{F}\mathbf{F}^T = \mathbf{U}_\mathbf{F} \mathbf{D}_\mathbf{F} \mathbf{U}_\mathbf{F}^T, \quad \mathbf{T}\mathbf{T}^T = \mathbf{U}_\mathbf{T} \mathbf{D}_\mathbf{T} \mathbf{U}_\mathbf{T}^T \quad (4)$$

and any eigenvalues significantly smaller than the others indicate degeneration in the direction of the corresponding eigenvectors. A straightforward choice of the metric to evaluate the degeneration is the eigenvalues. However, we found this metric difficult to interpret because its physical meaning is not clear. To accommodate this issue, we choose to project each row in \mathbf{F} and \mathbf{T} into the eigenspace

$$\mathbf{F}' = \mathbf{U}_\mathbf{F} \mathbf{F}, \quad \mathbf{T}' = \mathbf{U}_\mathbf{T} \mathbf{T} \quad (5)$$

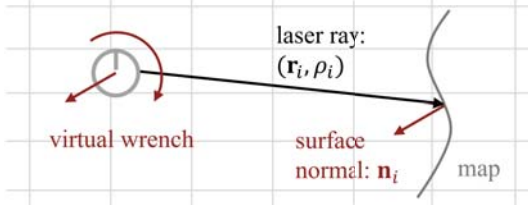


Fig. 2: An illustration of the visual wrench restraining the robot position and orientation.

and define the localizability vector $\mathbf{l}_F \in \mathbb{R}^3$ and $\mathbf{l}_T \in \mathbb{R}^3$ as

$$\mathbf{l}_{F,i} = \sum_{j=1}^m |\mathbf{F}'_{ij}|, \quad \mathbf{l}_{T,i} = \sum_{j=1}^m |\mathbf{T}'_{ij}| \quad (6)$$

meaning each element is the sum of absolute values of each row in \mathbf{F}' and \mathbf{T}' .

A closer look at Eqn. 2, 3 and 6 gives a more natural and intuitive interpretation. As illustrated in Fig. 2, we can interpret the position constraints as forces in the direction of \mathbf{n}_i (ignoring the signs) and the orientation constraints as torques in the direction of $\mathbf{r}_i \times \mathbf{n}_i$. Now the \mathbf{F} and \mathbf{T} are collections of wrenches (forces and torques) restraining the translation and rotation of the robot. Aligning with this picture, well-conditioned \mathbf{F} and \mathbf{T} indicate a *frictionless force-closure*, which is a term used in the field of manipulation mechanics to describe a solid grasp of an object. The characterization of a frictionless force-closure is to check whether the row vectors in \mathbf{F} and \mathbf{T} span the space of \mathbb{R}^3 [19]. Interestingly, this shares a similar idea of identifying degeneration using eigenvalues that are small. Furthermore, we can interpret the physical meaning of the localizability as the magnitude of accumulated virtual forces and torques gained from the measurements to restrain the uncertainty of pose estimation.

2) *Localizability of UWB Ranging*: The UWB sensor measures the distance from the anchor (attached to the environment) to the target (attached to the robot). Assuming the target is located at the origin of the robot body frame, we get the constraint equation

$$\mathcal{C}(\mathbf{x}, \mathbf{R}, \gamma) = \|\mathbf{x} - \mathbf{x}_a\|^2 - \|\gamma\|^2 = 0 \quad (7)$$

where $\mathbf{x}_a \in \mathbb{R}^3$ is the anchor position in the environment and $\gamma \in \mathbb{R}$ is the measured range. Following similar procedures, we obtain the force matrix \mathbf{F} for the UWB

$$\mathbf{F} = \frac{\mathbf{x} - \mathbf{x}_a}{\gamma} \quad (8)$$

(see Appendix II). Again \mathbf{F} can be treated as a collection of unit forces. In fact, there is only one column in \mathbf{F} and thus represents a single force in the direction from the anchor to the target. The force is later projected into the previously derived eigenspace to be compared with LiDAR localizability. On the other hand, since the sensor does not provide any information about the orientation, the torque matrix \mathbf{T} is trivially zero.

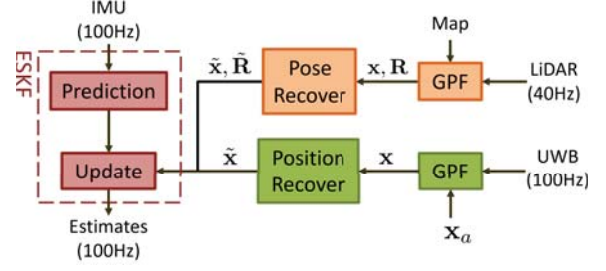


Fig. 3: Sensor fusion system overview. The green blocks indicate pipeline to process the UWB measurements and is described in detail in this paper. The red and orange blocks are pipelines of the ESKF and LiDAR fusion respectively.

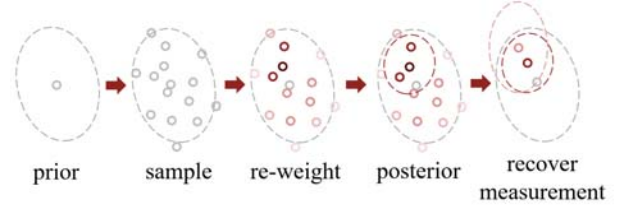


Fig. 4: An illustration of the GPF in 2D. Grey ellipse: uncertainty of prior belief. Dark red ellipse: the uncertainty of posterior. Light red ellipse: uncertainty of the recovered position measurement. The color of a particle encodes its weight with darker color corresponds to a higher weight.

B. Probabilistic Fusion of LiDAR and UWB

The fusion of IMU, LiDAR and the UWB is based on an Error State Kalman Filter (ESKF) (see Fig. 3). An ESKF is very similar to the well known Extended Kalman Filter (EKF), except it models the system dynamics in error states, which is beneficial when linearizing the system [20]. Basically, in the ESKF, the IMU measurements are integrated over time to predict the robot states. And the laser scans are matched to the prior map to recover a 6D pose measurement which is further used to update the prediction. Different from the LiDAR, the UWB ranges are converted to a 3D position measurement since the UWB doesn't contain any orientation information. After that, the recovered position is used to update the prediction similarly. Note that the update rate from LiDAR and UWB is different and depends on the data frequency. We encourage the readers to [11] for more details on ESKF and LiDAR fusion and only elaborate on the pipeline to process UWB data.

Specifically, a Gaussian Particle Filter (GPF) is used to convert the UWB ranges to a pose measurement as in [21]. First, a set of particles $\{\mathbf{x}_i \in \mathbb{R}^3 | i = 1, 2, \dots, N\}$ are drawn based on the position partition $(\bar{\mathbf{x}}, \bar{\Sigma}) \in (\mathbb{R}^3, \mathbb{S}^+)$ of the full prior belief which consists of position, orientation, velocity and so on. Additionally, each particle is assigned with a weighting factor

$$w_i = \exp \left[- \left(\frac{\|\mathbf{x}_i - \mathbf{x}_a\| - \gamma}{\sigma} \right)^2 \right] \quad (9)$$

where σ is the ranging noise of the UWB and is tuned by

hand in the experiments. This weighting factor measures how likely is each particle to be the true hypothesis. After that, the position posterior (\mathbf{x}, Σ) is found by computing the weighted mean and covariance of the set

$$\mathbf{x} = \frac{\sum w_i \mathbf{x}_i}{\sum w_i}, \quad \Sigma = \frac{\sum w_i (\mathbf{x}_i - \mathbf{x})(\mathbf{x}_i - \mathbf{x})^T}{\sum w_i} \quad (10)$$

With the prior and the posterior belief in hand, we differentiate them to recover a position measurement $(\tilde{\mathbf{x}}, \tilde{\Sigma})$

$$(\tilde{\mathbf{x}}, \tilde{\Sigma}) = (\mathbf{x}, \Sigma) \ominus (\bar{\mathbf{x}}, \bar{\Sigma}) \quad (11)$$

by inverting the Kalman update step

$$\tilde{\mathbf{x}} = \mathbf{K}^{-1}(\mathbf{x} - \bar{\mathbf{x}}) + \bar{\mathbf{x}} \quad (12)$$

$$\tilde{\Sigma} = (\Sigma^{-1} - \bar{\Sigma}^{-1})^{-1} \quad (13)$$

where \mathbf{K} is the Kalman gain computed as

$$\mathbf{K} = \bar{\Sigma}(\bar{\Sigma} + \tilde{\Sigma})^{-1} \quad (14)$$

Here the observation matrix is an identity and hence omitted.

Finally, $(\tilde{\mathbf{x}}, \tilde{\Sigma})$ is used to update the full state in the ESKF. Fig. 4 explains the process of converting UWB ranges into position measurements using a 2D example.

IV. EXPERIMENTS

A. Overview



Fig. 5: *Left*: The Smith Hall tunnel at CMU with the UWB anchor board placed on the ground. *Right*: The customized DJI M100 quadrotor.

Experiments are carried out inside the Smith Hall tunnel at CMU (shown in Fig. 5). The tunnel is of size $35\text{m} \times 2.4\text{m} \times 2.5\text{m}$ ($l \times w \times h$) with pipes on both sides. The prior map is obtained by aligning multiple local scans along the tunnel. The robot (see Fig. 5) is a customized DJI Matrice 100 quadrotor. It has a rotating Hokuyo UTM-30LX-EW LiDAR (40Hz, 30m range), a Microstrain IMU (100Hz), a Pozyx UWB target board (100Hz, 100m range with clear line-of-sight), and a DJI Manifold computer (2.32GHz). Note that the Hokuyo LiDAR is mounted on a continuously rotating motor ($180^\circ/\text{sec}$) and the laser scan is projected into the robot body frame using the encoder angles. There are other sensors such as GPS, compass and a gimbal camera that are not used in this work.

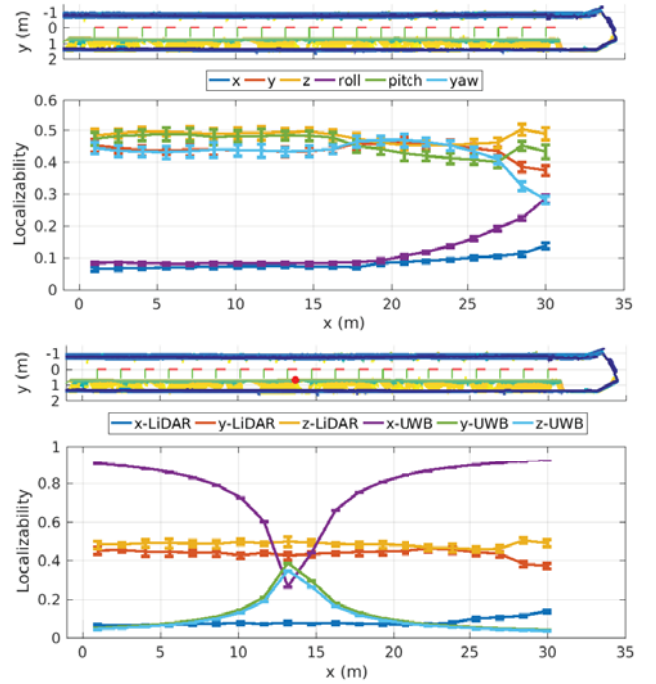


Fig. 6: *Top*: The LiDAR localizability along the tunnel. The upper plot is a top-down view of the pre-built map where the ground and ceiling points are cropped and the color encodes the height of remaining points. The red-green (x - y) frames indicate the 20 sampled positions. *Bottom*: A comparison of position localizability of the LiDAR and the UWB. The red dot marks the position of the UWB anchor in the tunnel.

B. Localizability inside the Tunnel

The LiDAR localizability is evaluated at 20 evenly sampled places along the tunnel (as shown in Fig. 6). Firstly, we define the map frame with x pointing along the tunnel and z pointing downward. Secondly, to simulate the measurements at each place, 4000 points are sampled uniformly within the range of 15 meters. We choose 4000 because that is about the amount of downsampled laser points used for localization per 180° rotation of the motor. And the effective range of LiDAR is decreased since distant points have nearly 90° reflection angle resulting in unreliable measurements. Then, at each point, a local surface is estimated by fitting a plane to its 20 nearest neighbors. Finally, using Eqn. 2-6, the localizability vector can be computed. The computation is repeated 10 times with different set of points and results are averaged. Fig. 6 shows a top-down view of the sampled poses and their localizability. In order to show the ‘strength’ of the localizability clearly in the later comparison, the values are scaled as

$$\mathbf{l}_i = \frac{\mathbf{l}_i}{\sum_i \mathbf{l}_i} \quad (i = 1, 2, 3)$$

It can be observed that the position and orientation localizability along x -axis is significantly smaller than the other two dimensions. This is because the position x is ambiguous along the tunnel except at the right end where a vertical

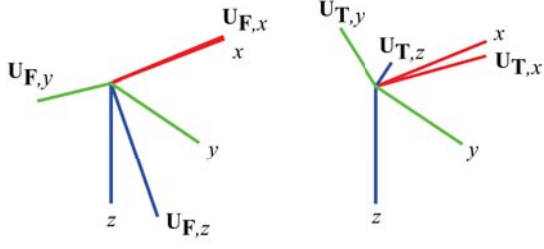


Fig. 7: An example of the eigenspace obtained from the 1st sampled place (near the left end of the tunnel). x -, y - and z -axis define the robot body frame. *Left*: The eigenspace of $\mathbf{F}\mathbf{F}^T$. *Right*: The eigenspace of $\mathbf{T}\mathbf{T}^T$.

wall restrains the position. Additionally, since the tunnel has an arc ceiling and almost identical width and height, the roll angle cannot be effectively constrained by LiDAR measurements. Fortunately, the orientation can be directly measured by the IMU thus roll angle is well-constrained after sensor fusion.

It's also worth to mention that the x -axis of the eigenspace is parallel to that of the body frame (see Fig. 7). That is because the x -axis in body frame is actually the degenerated direction. However, that is not necessarily the case for y and z if there is no significant difference in their constraint strength.

Considering the UWB, we project the force matrix into the fore-mentioned eigenspace, evaluate the localizability, and compare that with the LiDAR (see the bottom plot of Fig. 6). It is easy to see that the UWB compensates the LiDAR localizability along the x -axis, which means fusing the two sensors will make the estimation problem well-constrained. However, we observe a decrease of localizability in x near the anchor. This is a singular point where only position y and z are measured. Theoretically, additional anchors are needed to solve this issue. In practice, the singular point does not cause failure since the time of being under-constrained is short. Once the robot passes this position, the localizability in x increases and the robot can be localized again.

C. Tunnel Localization Test

The localization test is conducted by manually flying the robot from the map origin to the other end of the tunnel with an averaged speed of 0.7m/s. The UWB anchor board is placed a priori and its location is measured in the pre-built map. In this experiment, we control the usage of the UWB ranging data and compare the localization performance. When the UWB is disabled, the localization starts to drift shortly after the robot takes off. When the UWB ranging data is fused with LiDAR, the robot is able to successfully localize itself throughout the whole flight.

Fig. 8 shows the estimated trajectories, the prior map and the reconstructed map. Since the localization accuracy is difficult to measure without a motion capture system, we use the reconstructed map to qualitatively evaluate estimation accuracy. Although the reconstructed map shows larger noise than the prior map, the side structures are recovered, which indicates the localization is correct.

V. CONCLUSIONS

This paper presents a novel geometric degeneration modeling method that encodes the sensitivity of measurements w.r.t. robot poses. We find an analogy between the force-closure characterization and our method, which helps to explain the physical meaning of the localizability. Additionally, it is shown that the LiDAR and the UWB ranging sensor are complementary in terms of localizability and the presented fusion method is demonstrated to allow for robust localization inside real geometrically degenerated tunnels.

There are several directions for future work. Firstly, the constraint model of a localization problem is potentially generalizable to other sensors such as cameras. Secondly, it is still not clear how to compute the total localizability when multiple sensors of different modalities exist. In our experience, directly compositing constraints does not give reasonable results since sensor information may be redundant and the data comes at different time and frequency. Finally, although fusing UWB devices with LiDAR and IMU seems to be a feasible solution for localization inside tunnel-like environments, it requires the prior knowledge of the map and UWB positions, which will be an overhead for exploration tasks. Therefore, techniques for automatic calibration or localization of multiple UWB devices will be useful.

APPENDIX I

Without losing generality, we could always define the map frame to align with the robot body frame. In this way, (\mathbf{x}, \mathbf{R}) are small and can be treated as perturbations. Therefore the problem is reduced to evaluate how sensitive is ρ_i w.r.t. the perturbations (\mathbf{x}, \mathbf{R}) . This assumption allows using the small angle approximation $\mathbf{R} \approx \mathbf{I} + [\boldsymbol{\theta}]_{\times}$ to find the linearized constraint:

$$\begin{aligned} \bar{C}(\mathbf{x}, \boldsymbol{\theta}, \rho_i) &= \mathbf{n}_i^T (\mathbf{x} + (\mathbf{I} + [\boldsymbol{\theta}]_{\times}) \mathbf{r}_i \rho_i) + d_i \\ &= \mathbf{n}_i^T \mathbf{x} + \mathbf{n}_i^T \mathbf{r}_i \rho_i + \mathbf{n}_i^T [\boldsymbol{\theta}]_{\times} \mathbf{r}_i \rho_i + d_i \\ &= \mathbf{n}_i^T \mathbf{x} + \mathbf{n}_i^T \mathbf{r}_i \rho_i - \mathbf{n}_i^T [\mathbf{r}_i]_{\times} \boldsymbol{\theta} \rho_i + d_i \end{aligned} \quad (15)$$

Then based on the Implicit Function Theorem (IFT), we have

$$\frac{\partial \bar{C}}{\partial \mathbf{x}} d\mathbf{x} + \frac{\partial \bar{C}}{\partial \rho_i} d\rho_i = 0, \quad \frac{\partial \bar{C}}{\partial \boldsymbol{\theta}} d\boldsymbol{\theta} + \frac{\partial \bar{C}}{\partial \rho_i} d\rho_i = 0 \quad (16)$$

which implies

$$\begin{aligned} \frac{d\rho_i}{d\mathbf{x}} &= - \left(\frac{\partial \bar{C}}{\partial \mathbf{x}} \right) \left(\frac{\partial \bar{C}}{\partial \rho_i} \right)^{-1} = - \frac{\mathbf{n}_i^T}{\mathbf{n}_i^T \mathbf{r}_i} \\ \frac{d\rho_i}{d\boldsymbol{\theta}} &= - \left(\frac{\partial \bar{C}}{\partial \boldsymbol{\theta}} \right) \left(\frac{\partial \bar{C}}{\partial \rho_i} \right)^{-1} = - \frac{(\rho_i \mathbf{r}_i \times \mathbf{n}_i)^T}{\mathbf{n}_i^T \mathbf{r}_i} \end{aligned} \quad (17)$$

The derivatives are then stacked into matrix \mathbf{F} and \mathbf{T} .

APPENDIX II

Similarly, based on the IFT, we have

$$\frac{\partial \mathcal{C}}{\partial \mathbf{x}} d\mathbf{x} + \frac{\partial \mathcal{C}}{\partial \gamma} d\gamma = 0 \quad (18)$$

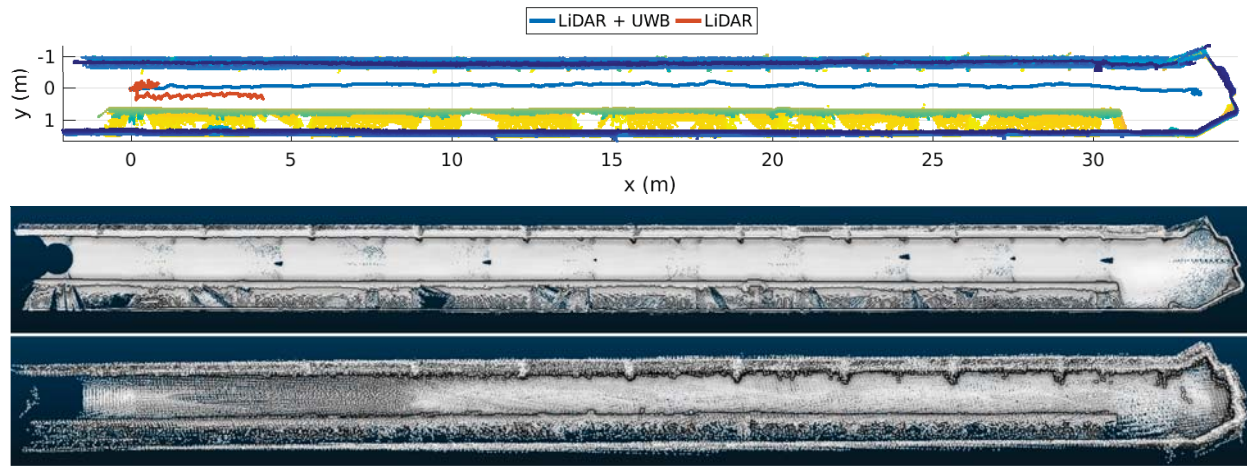


Fig. 8: *Up*: A comparison of estimated trajectories with/without fusion of the UWB ranging data. *Middle*: The ground truth map is built by matching multiple local scans using the ICP algorithm. *Bottom*: The reconstructed map is assembled by laser scans with estimated poses.

which implies

$$\frac{d\gamma}{dx} = - \left(\frac{\partial C}{\partial x} \right) \left(\frac{\partial C}{\partial \gamma} \right)^{-1} = \frac{x - x_a}{\gamma} \quad (19)$$

III. ACKNOWLEDGE

The authors are grateful to Xiangrui Tian and Qingxi Zeng for helping with the UWB configuration. This work is supported by the Department of Energy under award number DE-EM0004478.

REFERENCES

- [1] N. Roy and S. Thrun, "Coastal navigation with mobile robots," in *Advances in Neural Information Processing Systems*, 2000, pp. 1043–1049.
- [2] A. Diosi and L. Kleeman, "Uncertainty of line segments extracted from static SICK PLS laser scans," in *SICK PLS laser. In Australasian Conference on Robotics and Automation*, 2003.
- [3] A. Censi, "An accurate closed-form estimate of ICP's covariance," in *Robotics and Automation, 2007 IEEE International Conference on*. IEEE, 2007, pp. 3167–3172.
- [4] A. Censi, "On achievable accuracy for range-finder localization," in *Proceedings 2007 IEEE International Conference on Robotics and Automation*. IEEE, 2007, pp. 4170–4175.
- [5] A. Censi, "On achievable accuracy for pose tracking," in *Robotics and Automation, 2009. ICRA'09. IEEE International Conference on*. IEEE, 2009, pp. 1–7.
- [6] Z. Liu, W. Chen, Y. Wang, and J. Wang, "Localizability estimation for mobile robots based on probabilistic grid map and its applications to localization," in *Multisensor Fusion and Integration for Intelligent Systems (MFI), 2012 IEEE Conference on*. IEEE, 2012, pp. 46–51.
- [7] Y. Wang, W. Chen, J. Wang, and H. Wang, "Action selection based on localizability for active global localization of mobile robots," in *Mechatronics and Automation (ICMA), 2012 International Conference on*. IEEE, 2012, pp. 2071–2076.
- [8] Z. Liu, W. Chen, J. Wang, and H. Wang, "Action selection for active and cooperative global localization based on localizability estimation," in *Robotics and Biomimetics (ROBIO), 2014 IEEE International Conference on*. IEEE, 2014, pp. 1012–1018.
- [9] C. Hu, W. Chen, J. Wang, and H. Wang, "Optimal path planning for mobile manipulator based on manipulability and localizability," in *Real-time Computing and Robotics (RCAR), IEEE International Conference on*. IEEE, 2016, pp. 638–643.
- [10] J. Zhang, M. Kaess, and S. Singh, "On degeneracy of optimization-based state estimation problems," in *Robotics and Automation (ICRA), 2016 IEEE International Conference on*. IEEE, 2016, pp. 809–816.
- [11] W. Zhen, S. Zeng, and S. Scherer, "Robust localization and localizability estimation with a rotating laser scanner," in *2017 IEEE International Conference on Robotics and Automation (ICRA)*. Singapore: IEEE, 2017.
- [12] W. Vega-Brown, A. Bachrach, A. Bry, J. Kelly, and N. Roy, "Cello: A fast algorithm for covariance estimation," in *Robotics and Automation (ICRA), 2013 IEEE International Conference on*. IEEE, 2013, pp. 3160–3167.
- [13] A. Eudes and M. Lhuillier, "Error propagations for local bundle adjustment," in *Computer Vision and Pattern Recognition, 2009. CVPR 2009. IEEE Conference on*. IEEE, 2009, pp. 2411–2418.
- [14] P. Hansen, H. Alismail, P. Rander, and B. Browning, "Monocular visual odometry for robot localization in lng pipes," in *2011 IEEE International Conference on Robotics and Automation*. IEEE, 2011, pp. 3111–3116.
- [15] T. Özaslan, G. Loianno, J. Keller, C. J. Taylor, V. Kumar, J. M. Wozencraft, and T. Hood, "Autonomous navigation and mapping for inspection of penstocks and tunnels with mavs," *IEEE Robotics and Automation Letters*, vol. 2, no. 3, pp. 1740–1747, 2017.
- [16] C. Rizzo, V. Kumar, F. Lera, and J. L. Villarroel, "Rf odometry for localization in pipes based on periodic signal fadings," in *2014 IEEE/RSJ International Conference on Intelligent Robots and Systems*. IEEE, 2014, pp. 4577–4583.
- [17] C. Rizzo, F. Lera, and J. L. Villarroel, "A methodology for localization in tunnels based on periodic rf signal fadings," in *2014 IEEE Military Communications Conference*. IEEE, 2014, pp. 317–324.
- [18] Y.-D. Kim, G.-J. Son, H. Kim, C. Song, and J.-H. Lee, "Smart disaster response in vehicular tunnels: Technologies for search and rescue applications," *Sustainability*, vol. 10, no. 7, p. 2509, 2018.
- [19] R. M. Murray, *A mathematical introduction to robotic manipulation*. CRC press, 2017.
- [20] J. Sola, "Quaternion kinematics for the error-state kf," *Laboratoire d'Analyse et d'Architecture des Systemes-Centre national de la recherche scientifique (LAAS-CNRS), Toulouse, France, Tech. Rep*, 2012.
- [21] A. Bry, A. Bachrach, and N. Roy, "State estimation for aggressive flight in GPS-denied environments using onboard sensing," in *Robotics and Automation (ICRA), 2012 IEEE International Conference on*. IEEE, 2012, pp. 1–8.